Subaru High-z Exploration of Low-Luminosity Quasars (SHELLQs). II. Discovery of 32 Quasars and Luminous Galaxies at $5.7 < z \leq 6.8$

Yoshiki Matsuoka[1,2,3] , **Masafusa Onoue**[1, 2], **Nobunari Kashikawa**[1,2], **Kazushi Iwasawa**[4], **Michael A. Strauss**[5], **Tohru Nagao**[3], **Masatoshi Imanishi**[1, 2, 6], **Chien-Hsiu Lee**[6], **Masayuki Akiyama**[7], **Naoko Asami**[8], **James Bosch**[5], **Sébastien Foucaud**, **Hisanori Furusawa**[1], **Tomotsugu Goto**[10], **James E. Gunn**[5], **Yuichi Harikane**[11, 12], **Hiroyuki Ikeda**[1], **Takuma Izumi**[1], **Toshihiro Kawaguchi**[13], **Satoshi Kikuta**[2], **Kotaro Kohno**[14, 15], **Yutaka Komiyama**[1, 2], **Robert H. Lupton**[5], **Takeo Minezaki**[14], **Satoshi Miyazaki**[1, 2], **Tomoki Morokuma**[14], **Hitoshi Murayama**[16], **Mana Niida**[17], **Atsushi J. Nishizawa**[18], **Masamune Oguri**[12,15,16], **Yoshiaki Ono**[11], **Masami Ouchi**[11,16], **Paul A. Price**[5], **Hiroaki Sameshima**[19], **Andreas Schulze**[1], **Hikari Shirakata**[20], **John D. Silverman**[16], **Naoshi Sugiyama**[16, 21], **Philip J. Tait**[6], **Masahiro Takada**[16], **Tadafumi Takata**[1, 2], **Masayuki Tanaka**[1, 2], **Ji-Jia Tang**[22], **Yoshiki Toba**[22], **Yousuke Utsumi**[23] and **Shiang-Yu Wang**[22]

[1]National Astronomical Observatory of Japan, Mitaka, Tokyo 181-8588, Japan.

[2]Department of Astronomical Science, Graduate University for Advanced Studies (SOKENDAI), Mitaka, Tokyo 181-8588, Japan.

[3]Research Center for Space and Cosmic Evolution, Ehime University, Matsuyama, Ehime 790-8577, Japan.

[4]ICREA and Institut de Ciències del Cosmos, Universitat de Barcelona, IEEC-UB, Martí i Franquès, 1, 08028 Barcelona, Spain.

[5]Princeton University Observatory, Peyton Hall, Princeton, NJ 08544, USA.

[6]Subaru Telescope, Hilo, HI 96720, USA.

[7]Astronomical Institute, Tohoku University, Aoba, Sendai, 980-8578, Japan.

[8]Japan Professional School of Education, Chiyoda, Tokyo 101-0041, Japan.

[9]Department of Physics and Astronomy, Shanghai JiaoTong University, Shanghai 200240, China.

[10]Institute of Astronomy and Department of Physics, National Tsing Hua University, Hsinchu 30013, Taiwan.

[11]Institute for Cosmic Ray Research, The University of Tokyo, Kashiwa, Chiba 277-8582, Japan

[12]Department of Physics, Graduate School of Science, The University of Tokyo, Bunkyo, Tokyo 113-0033, Japan

[13]Department of Economics, Management and Information Science, Onomichi City University, Onomichi, Hiroshima 722-8506, Japan.

[14]Institute of Astronomy, The University of Tokyo, Mitaka, Tokyo 181-0015, Japan.

[15]Research Center for the Early Universe, University of Tokyo, Tokyo 113-0033, Japan.

[16]Kavli Institute for the Physics and Mathematics of the Universe, WPI, The University of Tokyo,Kashiwa, Chiba 277-8583, Japan.

[17]Graduate School of Science and Engineering, Ehime University, Matsuyama, Ehime 790-8577, Japan.

[18]Institute for Advanced Research, Nagoya University, Furo-cho, Chikusa-ku, Nagoya 464-8602, Japan.

[19]Koyama Astronomical Observatory, Kyoto-Sangyo University, Kita, Kyoto, 603-8555, Japan.

[20]Department of Cosmosciences, Graduates School of Science, Hokkaido University, N10 W8, Kitaku, Sapporo 060-0810, Japan.

[21]Graduate School of Science, Nagoya University, Furo-cho, Chikusa-ku, Nagoya 464-8602, Japan.

[22]Institute of Astronomy and Astrophysics, Academia Sinica, Taipei, 10617, Taiwan.

[23]Hiroshima Astrophysical Science Center, Hiroshima University, Higashi-Hiroshima, Hiroshima 739-8526, Japan.

*E-mail: yk.matsuoka@cosmos.ehime-u.ac.jp

Abstract

We present spectroscopic identification of 32 new quasars and luminous galaxies discovered at $5.7 < z \leq 6.8$. This is the second in a series of papers presenting the results of the Subaru High-z Exploration of Low-Luminosity Quasars (SHELLQs) project, which exploits the deep multi-band imaging data produced by the Hyper Suprime-Cam (HSC) Subaru Strategic Program survey. The photometric candidates were selected by a Bayesian probabilistic algorithm, and then observed with spectrographs on the Gran Telescopio Canarias and the Subaru Telescope. Combined with the sample presented in the previous paper, we have now identified 64 HSC sources over about 430 deg^2, which include 33 high-z quasars, 14 high-z luminous galaxies, 2 [O III] emitters at $z \sim 0.8$, and 15 Galactic brown dwarfs. The new quasars have considerably lower luminosity ($M_{1450} \sim -25$ to -22 mag) than most of the previously known high-z quasars. Several of these quasars have luminous ($> 10^{43}$ erg s^{-1}) and narrow (< 500 km s^{-1}) Lyα lines, and also a possible mini broad absorption line system of N V λ1240 in the composite spectrum, which clearly separate them from typical quasars. On the other hand, the high-z galaxies have extremely high luminosity ($M_{1450} \sim -24$ to -22 mag) compared to other galaxies found at similar redshift. With the discovery of these new classes of objects, we are opening up new parameter spaces in the high-z Universe. Further survey observations and follow-up studies of the identified objects, including the construction of the quasar luminosity function at $z \sim 6$, are ongoing.

Key words: dark ages, reionization, first stars — galaxies: active — galaxies: high-redshift — quasars: general — quasars: supermassive black holes

1 Introduction

High-z quasars are a unique and useful probe of the early Universe in many aspects. The progress of cosmic reionization has been measured by the strength of H I absorption in background quasar spectra, which is very sensitive to the neutral fraction of the intergalactic medium (IGM; Gunn & Peterson 1965; Fan et al. 2006a). Stringent constraints on the seed population and initial growth of supermassive black holes (SMBHs) can be obtained from their mass function, in particular their maximum mass, as a function of redshift (e.g., Volonteri 2012; Ferrara et al. 2014; Madau et al. 2014). We can also learn about

the formation of their host galaxies, which is thought to have happened in the highest density peaks of the underlying dark matter distribution in the early phase of cosmic history.

There has been great progress in the quest for high-z quasars[1] in the last two decades. This progress was made possible by the advent of wide-field (≥ 1000 deg^2) surveys in the optical or near-infrared (IR) bands, such as SDSS (York et al. 2000), the Canada-France-Hawaii Telescope Legacy Survey,

---

[1] Hereafter, "high-z" denotes $z > 5.7$, where quasars are observed as i-band dropouts in the Sloan Digital Sky Survey (SDSS) filter system (Fukugita et al. 1996).

the United Kingdom Infrared Telescope (UKIRT) Infrared Deep Sky Survey (UKIDSS; Lawrence et al. 2007), the Panoramic Survey Telescope & Rapid Response System 1 (Pan-STARRS1; Kaiser et al. 2010) 3π survey, the Dark Energy Survey (Dark Energy Survey Collaboration 2016), and the Visible and Infrared Survey Telescope for Astronomy (VISTA) Kilo-degree Infrared Galaxy (VIKING). High-z quasar discoveries from the above and other projects are reported in Fan et al. (2000, 2001a, 2003, 2004, 2006b), Jiang et al. (2008, 2009, 2015, 2016), Willott et al. (2005, 2007, 2009, 2010ab), Mortlock et al. (2011), Bañados et al. (2014, 2016), Reed et al. (2015, 2017), Venemans et al. (2013, 2015ab), Goto (2006), Carnall et al. (2015), Kashikawa et al. (2015), Kim et al. (2015), Wu et al. (2015), and Wang et al. (2017).

More than 100 high-z quasars are known today (Bañados et al. 2016), with the most distant object found at $z = 7.085$ (Mortlock et al. 2011). However, most of these quasars have redshifts $z < 6.5$ and absolute magnitudes $M_{1450} < -24$ mag, while higher redshifts and fainter magnitudes are still poorly explored. The known quasars must be just the tip of an iceberg predominantly comprised of faint quasars and AGNs, which may be a significant contributor to reionization, and may represent the more typical mode of SMBH growth in the early Universe.

This paper is the second in a series presenting the results of the Subaru High-z Exploration of Low-Luminosity Quasars (SHELLQs) project, which exploits multi-band photometry data produced by the Hyper Suprime-Cam (HSC) Subaru Strategic Program (SSP) survey. The first results were presented in Matsuoka et al. (2016; hereafter Paper I), where we described the motivation and strategy of the project in detail, as well as the discovery of 15 quasars and luminous galaxies at $5.7 < z < 6.9$ from the initial 80 deg^2 of the survey. In the present paper, we report the discovery of an additional 24 quasars and 8 luminous galaxies at $z > 5.7$, from about 430 deg^2 (including the previous 80 deg^2) of the survey. The spectroscopic follow-up campaign on the present survey area is still ongoing, whose results will be presented in forthcoming papers. We are also working to construct quasar luminosity function at $z \sim 6$, which will be presented in a separate paper.

This paper is organized as follows. We briefly describe the photometric candidate selection in §2, while a more complete description is found in Paper I. The spectroscopic follow-up observations are described in §3. The quasars and galaxies we have discovered are presented and discussed in §4. The summary appears in §5. We adopt the cosmological parameters $H_0 = 70$ km s^{-1} Mpc^{-1}, $\Omega_M = 0.3$, and $\Omega_\Lambda = 0.7$. All magnitudes in the optical and NIR bands are presented in the AB system (Oke & Gunn 1983). Magnitudes refer to point spread function (PSF) magnitudes (see §2.1) corrected for Galactic extinction (Schlegel et al. 1998), unless otherwise noted. In what follows,

we refer to z-band magnitudes with the AB subscript ("z_{AB}"), while redshift z appears without a subscript.

2 Photometric Candidate Selection

Our quasar candidates were selected in essentially the same way as in Paper I, so we only briefly describe the relevant procedure here, highlighting a few minor changes we made. The reader is referred to Paper I for a more complete description of our selection.

2.1 The Subaru HSC-SSP Survey

The SHELLQs project is based on the imaging data collected by the Subaru SSP survey with the HSC (Miyazaki et al. 2012, Miyazaki et al., in prep.), a wide-field camera installed on the Subaru 8.2 m telescope. HSC has a nearly circular field of view of $1°.5$ diameter, covered by 116 2K × 4K Hamamatsu fully depleted CCDs, with the pixel scale of $0''.17$. The survey has three layers: the Wide layer is observing 1400 deg^2 mostly along the celestial equator, with the 5σ target depths of (g_{AB}, r_{AB}, i_{AB}, z_{AB}, y_{AB}) = (26.5, 26.1, 25.9, 25.1, 24.4) mag measured in $2''.0$ apertures, while the Deep and the UltraDeep layers are observing smaller areas (27 and 3.5 deg^2) down to deeper limiting magnitudes (r_{AB} = 27.1 and 27.7 mag, respectively). A full description of the survey may be found in Aihara et al. (in prep.). The first public data release (DR1) took place in 2017 February, which includes the data taken in the first 1.7 years (2014 March to 2015 November) of the survey, covering 108 deg^2 of the Wide layer and the Deep and UltraDeep layers to intermediate depths (Aihara et al. 2017). The median seeing during the above observing period was $0''.5 - 0''.8$, depending on filter. The DR1 Wide layer reaches limiting magnitudes consistent with the above target values, while we are still accumulating exposures in the Deep and UltraDeep layers to reach the final target depths.

The results presented in this paper were drawn from imaging data observed before 2016 April, i.e., a newer dataset than contained in DR1. We used about 430 deg^2 of the Wide layer, in which we have more than one exposure in the i, z, and y-bands.[2] The total integration time per pointing in each of the (i, z, y) bands in the Wide layer is 20 minutes, divided into six individual exposures with different dither positions. Data reduction was performed with the dedicated pipeline hscPipe (version 4.0.1 and 4.0.2; Bosch et al., in prep.) derived from the Large Synoptic Survey Telescope software pipeline (Jurić et al. 2015), for all the standard procedures including bias subtraction, flat fielding with dome flats, stacking, astrometric and pho-

---

[2] The quasar selection presented in this work was not restricted to the areas observed to the planned full depth. We didn't use the higher-quality data from the Deep and UltraDeep layers, which are available over a small fraction of the Wide field.

tometric calibrations, as well as source detection and measurements. The astrometric and photometric calibrations are tied to the Pan-STARRS1 system (Schlafly et al. 2012; Tonry et al. 2012; Magnier et al. 2013; Chambers et al. 2016; Flewelling et al. 2016). We use the PSF magnitude (m_{AB}) and the CModel magnitude ($m_{CModel,AB}$), which are measured by fitting the PSF models and two-component, PSF-convolved galaxy models to the source profile, respectively (Abazajian et al. 2004). These magnitudes have been corrected for Galactic extinction (Schlegel et al. 1998).

2.2 Candidate Selection

We start our candidate selection from the HSC-SSP source catalog over the Wide layer. The initial query from the database is as follows:

$$(z_{AB} < 24.5 \text{ and } \sigma_z < 0.155 \text{ and } i_{AB} - z_{AB} > 1.5$$
$$\text{and } z_{AB} - z_{CModel,AB} < 0.15) \qquad (1)$$

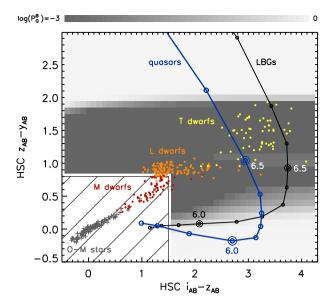or

$$(y_{AB} < 24.0 \text{ and } \sigma_y < 0.155 \text{ and } z_{AB} - y_{AB} > 0.8$$
$$\text{and } y_{AB} - y_{CModel,AB} < 0.15). \qquad (2)$$

We reject objects with the critical quality flags detailed in Paper I. Throughout this paper, (i_{AB}, z_{AB}, y_{AB}) refer to PSF magnitudes, and (σ_i, σ_z, σ_y) refer to their errors. The conditions of Equation 1 select i-band dropouts at $z \sim 6$, while those of Equation 2 select z-band dropouts at $z \sim 7$. The color cuts are used to remove relatively blue stars with O to early-M spectral types (see Figure 1), while the difference between the PSF and CModel magnitudes is used to exclude extended sources. We changed the extendedness cut from $m_{AB} - m_{CModel,AB} < 0.30$ in Paper I to < 0.15 in the present work, so that galaxies are removed more efficiently; we discuss this issue later in this paper. After the database query, we further remove low-z interlopers with more than 3σ detection in the g or r band.

Next, an automatic image checking procedure is run on stacked images and per-visit images (i.e., images of individual exposures before stacking) of the above sources. This procedure uses Source Extractor (Bertin & Arnouts 1996) in the double-image mode, with the stacked image as the detection reference. If any of the per-visit photometric measurements deviate by more than three times the measurement error from the stacked photometry, the source is eliminated. We also reject sources with too compact, diffuse, or elliptical profiles to be celestial point sources on the stacked images. The eliminated sources are mostly cosmic rays, moving or transient sources, and image artifacts.

The red HSC sources selected above are matched to the UKIDSS and VIKING catalogs within $1''.0$, which provides J, H, and K-band photometry. The present work utilizes the

Fig. 1. HSC $i_{AB} - z_{AB}$ and $z_{AB} - y_{AB}$ colors of high-z quasars (blue line) and galaxies (black line), as well as Galactic stars and brown dwarfs (crosses and dots). The models and references used to compute these colors are described in Paper I. The open circles along the blue and black lines represent redshifts in steps of 0.1, with $z = 6.0$ and 6.5 marked by the larger circles. The hatched area in lower left indicates the color space excluded from the SSP database query in the first step of the quasar selection (§2.2). The grey scale represents the Bayesian quasar probability P_Q^B (the color bar is found at the top) over this plane, for a source magnitude of $z_{AB} = 24.0$ mag and 5σ limiting magnitudes of (i_{AB}, z_{AB}, y_{AB}) = (26.5, 25.5, 25.0) mag. Galaxy models are not included in our algorithm at present.

UKIDSS data release 10 and the VIKING data release 4. The UKIDSS data cover almost the entire HSC survey fields, while the available VIKING data cover 30–40 % of the HSC survey footprint used in this work.

We use a template-based Bayesian probabilistic method, which selects quasar candidates from the above sample of red HSC sources. Similar methods of spectral energy distribution (SED) fitting have been used in other quasar surveys (e.g., Reed et al. 2017), while more advanced Bayesian treatment, e.g., with surface density priors (Mortlock et al. 2012), is not frequently seen in the literature. For each source, we calculate the Bayesian probability (P_Q^B) of being a high-z quasar rather than a contaminating brown dwarf, based on models of SED and surface density as a function of magnitude. Galaxy models are not included in the algorithm at present. The quasar SED models were created by stacking the SDSS spectra of 340 bright quasars at $z \simeq 3$, where the quasar selection is fairly complete (Richards et al. 2002; Willott et al. 2005), and correcting for the effect of IGM absorption (Songaila 2004). The quasar surface density was modeled based on the luminosity function taken from Willott et al. (2010b). A more detailed description about our Bayesian algorithm may be found in Paper I.

We keep those sources with $P_Q^B > 0.1$ in the sample of candidates, while removing sources with lower quasar probability.

The rather low value of the threshold $P_Q^B = 0.1$ was chosen to ensure that we would not throw away any possible candidates. We found that the actual P_Q^B distribution is bimodal, with only a small fraction falling in $0.1 < P_Q^B < 0.9$ (see §4.5), so our results are insensitive to the exact value of this cut. As we will see below, the bimodal P_Q^B distribution is populated mostly by high-z quasars at $P_Q^B \simeq 1$ and brown dwarfs at $P_Q^B \simeq 0$. This indicates that quasars and brown dwarfs occupy distinct regions of the color space, and HSC (and UKIDSS/VIKING) photometry is sufficiently accurate to separate these two populations, down to the limiting magnitude of our quasar survey.

Finally, we inspect the images of all the candidates by eye and reject additional problematic sources. Both stacked and per-visit images are used for this purpose. The sources rejected at this stage include those close to bright stars, cosmic rays, and moving objects overlooked in the above automatic procedure.

In the present survey area covering 430 deg^2, we had roughly 300,000 red point sources meeting the database query conditions (Equations 1 and 2) and undetected in the g and r bands. The vast majority of them ($\sim$97 %) were eliminated by the automatic image checking procedure, and the Bayesian algorithm selected 261 final candidates with $P_Q^B > 0.1$. Among them, we put highest priority for follow-up spectroscopy on the 60 candidates with reddest colors ($i_{AB} - z_{AB} > 2.0$ or $z_{AB} - y_{AB} > 0.8$; see Figure 1), relatively bright magnitudes ($z_{AB} < 24$ mag), and detection in more than a single band or a single exposure.

2.3 Recovery of Known Objects

In the 430 deg^2 surveyed in this paper, there are ten high-z quasars discovered by previous surveys. We have recovered seven of these quasars (CFHQS $J0210 - 0456$, CFHQS $J0216 - 0455$, CFHQS $J0227 - 0605$, SDSS $J1602 + 4228$, IMS $J2204 + 0012$, VIMOS2911001793, and SDSS $J2228 + 0110$, following the naming convention of Bañados et al. 2016), all of which have $P_Q^B = 1.00$. On the other hand, two quasars (SDSS $J0836 + 0054$ and VIK $J1148 + 0056$) have relatively low redshifts ($z = 5.81$ and 5.84, respectively) and bluer HSC colors ($i - z < 1.5$) than our selection threshold. The remaining quasar (VIK $J0839 + 0015$) was dropped from the selection, because it has r-band detection ($r_{AB} = 25.16 \pm 0.11$ mag) in the HSC catalog. This quasar is at $z = 5.84$ and bright also in the i band ($i_{AB} = 22.86 \pm 0.01$ mag), so the r-band detection may be real. Alternatively, the r-band flux peak may be an artifact due to the halo around a saturated star, at $\sim 13''$ away from the quasar.

Our quasar selection algorithm was run on all HSC data observed before 2016 April, so the present quasar candidates supersede those in Paper I. Because the HSC data reduction pipeline is improving continuously, and because we've made a minor change of the selection criteria as mentioned above,

the candidate lists in a given observed field may vary from one round of selection to another. In Paper I, we reported spectroscopic identification of nine high-z quasars, six high-z galaxies, and one brown dwarf. We found that the present selection recovers eight quasars and two galaxies from the above sample. $J2232 + 0012$, which we classified as a quasar based on the very high luminosity ($\sim 10^{44.1}$ erg s^{-1}) of its narrow Lyα line, was dropped from the candidates, because its extendedness ($z_{AB} - z_{CModel,AB} = 0.156$) is slightly above our new threshold (0.150; see above). The two galaxies $J0857 + 0142$ and $J0848 + 0045$ were dropped from the quasar candidates for the same reason. The three remaining sources, i.e., the galaxies $J0210 - 0523$ and $J0215 - 0555$ and the brown dwarf $J0850 + 0012$, have lower P_Q^B values than in Paper I, and didn't meet the selection criterion ($P_Q^B > 0.1$).

3 Spectroscopy

Since the discovery reported in Paper I, we took optical spectra of 48 additional unidentified quasar candidates, using the Optical System for Imaging and low-Intermediate-Resolution Integrated Spectroscopy (OSIRIS; Cepa et al. 2000) mounted on the Gran Telescopio Canarias (GTC), and the Faint Object Camera and Spectrograph (FOCAS; Kashikawa et al. 2002) mounted on Subaru. The observations were carried out in the 2016 Spring and Fall semesters. Roughly the brighter half of the candidates were observed with OSIRIS, while the fainter candidates were observed with FOCAS. We prioritized observations in such a way that the targets with brighter magnitudes and higher P_Q^B were observed at the earlier opportunities. The journal of these discovery observations is presented in Table 1. The details of the observations are described in the following sections.

3.1 GTC/OSIRIS

GTC is a 10.4-m telescope located at the Observatorio del Roque de los Muchachos in La Palma, Spain. Our program was awarded 14.4 and 21.5 hours in the 2015B and 2016A semesters, respectively (GTC19-15B and GTC4-16A; Iwasawa et al.). We used OSIRIS with the R2500I grism and $1''.0$-wide long slit, which provides spectral coverage from $\lambda_{obs} = 0.74$ to 1.0 μm with a resolution $R \sim 1500$. The observations were carried out in queue mode on dark and gray nights, with mostly photometric (sometimes spectroscopic) sky conditions and the seeing $0''.6 - 1''.2$. The data were reduced using the Image Reduction and Analysis Facility (IRAF). Bias correction, flat fielding with dome flats, sky subtraction, and 1d extraction were performed in the standard way. The wavelength was calibrated with reference to sky emission lines. The flux calibration was tied to white dwarf standard stars (Feige 110, Feige 66, G191-

B2B, GD 140, or Ross 640) observed on the same nights. We corrected for slit losses by scaling the spectra to match the HSC magnitudes in the z and y bands for the i- and z-band dropouts, respectively.

3.2 Subaru/FOCAS

Our program was awarded five nights each in the S16A and S16B semesters (S16A-076 and S16B-071I; Matsuoka et al.) with the Subaru 8.2-m telescope. The latter program (S16B-071I) has been approved as a Subaru intensive program, for which a total of 20 nights will be allocated during the S16B – S18A semesters. We used FOCAS in the multi-object spectrograph mode with the VPH900 grism and SO58 order-sorting filter. The widths of the slitlets were set to $1''.0$. This configuration provides spectral coverage from $\lambda_{\mathrm{obs}} = 0.75$ to 1.05 μm with a resolution $R \sim 1200$. All the observations were carried out on grey nights. A few of these nights were occasionally affected by cirrus and poor seeing ($\lesssim 2''.0$), while the weather was fairly good with seeing $0''.5 - 1''.0$ for the rest of the observations.

The data were reduced with IRAF using the dedicated FOCASRED package. Bias correction, flat fielding with dome flats, sky subtraction, and 1d extraction were performed in the standard way. The wavelength was calibrated with reference to the sky emission lines. The flux calibration was tied to white dwarf standard stars (Feige 110 and G191-B2B) observed on the same nights as the targets. We corrected for slit losses in the same way as in the OSIRIS data reductions.

4 Results and Discussion

Figures 2 – 8 present the reduced spectra of the 48 quasar candidates. As we describe in detail below, we identified 24 high-z quasars, 8 high-z galaxies, 2 strong [O III] emitters at $z \sim 0.8$, and 14 brown dwarfs. Their photometric properties are summarized in Table 2. Note that the astrometric accuracy of the HSC-SSP data is estimated to be $\lesssim 0''.1$ (root mean square; Aihara et al. 2017). Table 2 also lists the updated magnitudes and $P_{\mathrm{Q}}^{\mathrm{B}}$ of the 16 objects presented in Paper I, measured with the present version of the HSC data reduction pipeline. Note that some of the objects in this table do not meet our latest quasar selection criteria, due either to the improvement of the HSC photometry or to our minor changes in the selection criteria (see §2.2). We clarify this point below whenever necessary. We have now spectroscopically identified 64 HSC sources in Paper I and this work, which include 33 high-z quasars, 14 high-z galaxies, 2 [O III] emitters, and 15 brown dwarfs. Six of these sources are detected in the J, H, and/or K band, as summarized in Table 3.

4.1 Quasars and Possible Quasars

We identified 24 new quasars and possible quasars at $5.9 < z \lesssim 6.8$, as displayed in Figures 2 – 4 and listed in the first section of Table 4. The highest-z quasar, $J1429-0104$, was the only z-band dropout we took a spectrum of. This quasar has two emission peaks, whose wavelengths are close to the expected positions of Lyα and N V $\lambda1240$ at $z = 6.8$. The dip between the two emission lines is likely caused by a broad absorption line (BAL) system of N V. The majority of the objects in Figures 2 – 4 exhibit characteristic spectral features of high-z quasars, namely, strong and broad Lyα and in some cases N V $\lambda1240$, blue rest-UV continua, and sharp continuum breaks just shortward of Lyα. On the other hand, several objects have considerably narrower Lyα than do typical quasars. As discussed later in this section, we classify these objects with narrow Lyα as (possible) quasars, given their high Lyα luminosity, and possible mini BAL feature of N V found in their composite spectrum.

The redshifts of the above objects were determined from the Lyα lines, assuming that the observed line peaks correspond to the intrinsic Lyα wavelength (1216 Å in the rest frame). This assumption is not always correct, due to the strong IGM H I absorption, so the redshifts presented here (Table 4) must be interpreted with caution.

We measured the rest-frame UV absolute magnitudes (M_{1450}) of these objects and the 9 quasars presented in Paper I, as follows. All the spectra in Paper I were re-scaled to match the latest HSC photometry used in this work. For every object, we determined the wavelength range of a continuum window, which is relatively free from strong sky emission lines; this is 9000 – 9300 Å in the most cases, while the longer wavelengths between 9600 Å and 9900 Å were chosen for the objects at $z > 6.4$. We calculated the inverse-variance-weighted mean of the flux in the continuum window, which was then extrapolated to $\lambda_{\mathrm{rest}} = 1450$ Å, by assuming a power-law continuum slope of $\alpha = -1.5$ ($F_\lambda \propto \lambda^\alpha$; e.g., Vanden Berk et al. 2001). Since the continuum windows (corresponding to $\lambda_{\mathrm{rest}} = 1265 - 1345$ Å) are close to $\lambda_{\mathrm{rest}} = 1450$ Å, the derived M_{1450} values are not sensitive to the exact value of α.

We also measured the line properties (rest-frame equivalent width [EW], full width at half maximum [FWHM], and luminosity) of Lyα for the objects in this paper and Paper I, as follows. For the twelve objects with narrow Lyα ($J0905+0300$, $J0217-0208$, $J2201+0155$, $J1423-0018$, $J1440-0107$, $J0235-0532$, $J1416+0015$, $J1417+0117$, $J0853+0139$ in this work, and $J2232+0012$, $J2228+0128$, $J1207-0005$ from Paper I), we measured the line properties with the continuum levels estimated by averaging all the pixels redward of Lyα, with inverse-variance weighting. For $J0859+0022$ from Paper I, we similarly measured the above properties for the strong Lyα and N V $\lambda1240$ lines. For the remaining objects, we measured the properties of the broad Lyα + N V complex, with
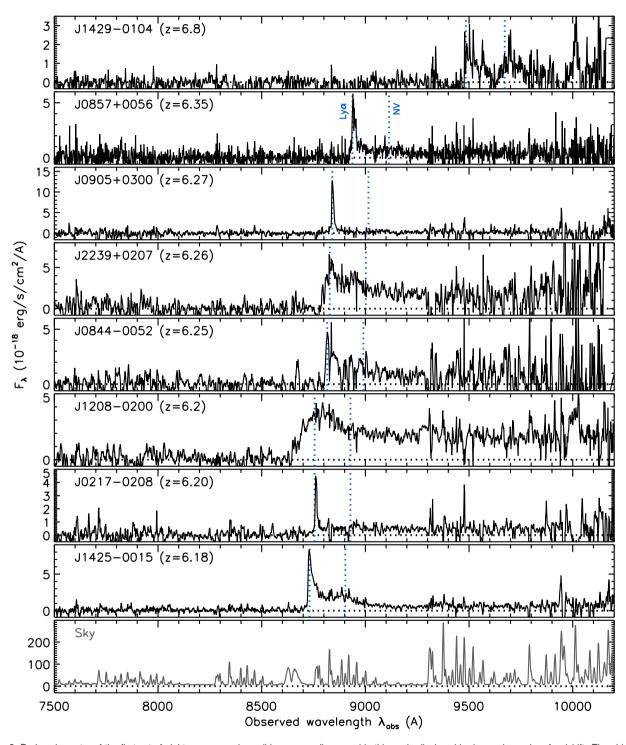
Fig. 2. Reduced spectra of the first set of eight quasars and possible quasars discovered in this work, displayed in decreasing order of redshift. The object name and the estimated redshift are indicated at the top left corner of each panel. The blue dotted lines mark the expected positions of the Lyα and Nv $\lambda 1240$ emission lines, given the redshifts. The spectra were smoothed using inverse-variance weighted means over $3 - 9$ pixels (depending on the S/N), for display purposes. The bottom panel displays a sky spectrum, as a guide to the expected noise.

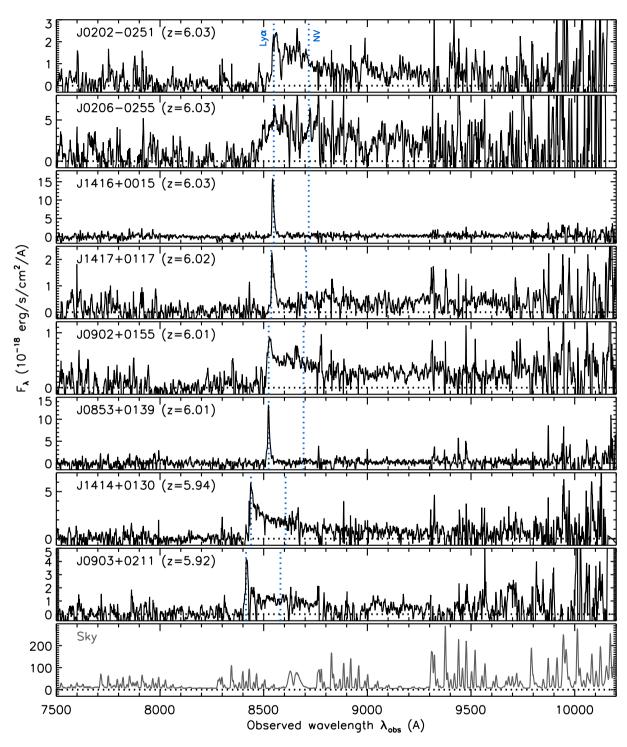**Fig. 3.** Same as Figure 2, but for the second set of eight quasars and possible quasars.

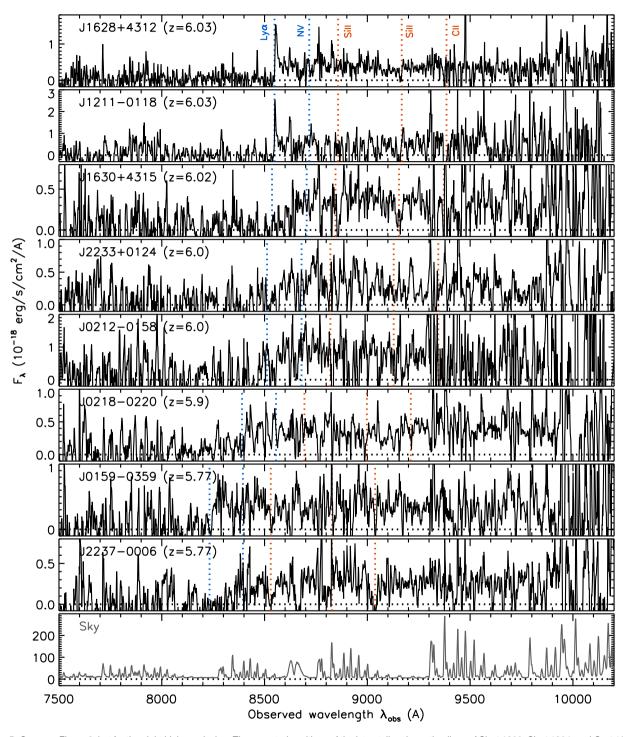**Fig. 4.** Same as Figure 2, but for the last set of eight quasars and possible quasars.

Fig. 5. Same as Figure 2, but for the eight high-z galaxies. The expected positions of the interstellar absorption lines of Si ɪɪ $\lambda1260$, Si ɪɪ $\lambda1304$, and C ɪɪ $\lambda1335$ are marked by the red dotted lines.
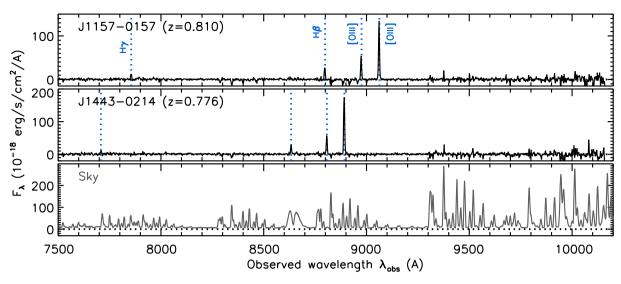
Fig. 6. Same as Figure 2, but for the two [O III] emitters at $z \sim 0.8$. The expected positions of Hγ, Hβ, and two [O III] lines (λ4959 and λ5007) are marked by the dotted lines.

the local continuum defined by the extrapolation of the above power-law continuum (with the assumed slope of $\alpha = -1.5$). Due to the difficulty in defining the accurate continuum levels, the measurements for these objects should be regarded as only approximate. The resultant line properties are summarized in Table 4. Figure 9 displays M_{1450} and the rest-frame Lyα EWs of the above quasars, as well as those of the high-z galaxies with clear Lyα emission described in §4.2. The quasars broadly follow the best-fit relation of AGNs at lower redshifts (Dietrich et al. 2002), if we assume IGM absorption of $\sim$50 % of the Lyα emission. A detailed analysis of the derived line properties will be presented in a future paper.

It is challenging to pin down the excitation sources of the narrow Lyα lines, observed in the above twelve objects. These narrow lines are unambiguously Lyα at $z \sim 6$, since we observe a clear continuum break just blueward of this line in every object, which is caused by the IGM H I absorption. We created a high-S/N composite spectrum by stacking the spectra of all twelve objects. The individual spectra were converted to the rest frame and normalized to $M_{1450} = -22.5$ mag, and then stacked together with inverse-variance weighting. Since the twelve objects have similar continuum flux and S/N to each other, the composite spectrum has roughly equal contribution from every object in its continuum.

As displayed in Figure 10, we see a clear continuum break and asymmetric Lyα line in the composite spectrum. The Lyα has a very narrow profile with a FWHM of $\sim$300 km s^{-1} and the rest-frame EW of $\sim$20 Å, but the intrinsic width may be as much as twice the observed value, due to IGM absorption. On the other hand, small redshift errors will broaden the Lyα in the composite, so the measured FWHM is an upper limit. For comparison, candidate type-II quasars presented by Alexandroff et al. (2013) have typical FWHMs of ~ 1000 km s^{-1} in the narrow

component of Lyα. While no N V λ1240 emission is present in the composite spectrum, we observe a small absorption feature just blueward of the expected wavelength of N V. This feature is not clearly seen in any of the individual spectra. No stellar or interstellar absorption is known at this wavelength (see, e.g., the composite spectrum of Lyman break galaxies [LBGs] in Shapley et al. 2003), so this feature may be a mini BAL caused by N V. We note that a possibly similar Lyα-only AGN, which has associated C IV λ1549 absorption systems but no metal-line emission such as N V and C IV, was found at $z = 2.5$ in SDSS (Hall et al. 2004). This composite spectrum is also reminiscent of those of type-II quasars (Stern et al. 2002; Mainieri et al. 2005; Martínez-Sansigre et al. 2006; Alexandroff et al. 2013) or radio galaxies (McCarthy 1993), which generally have very high Lyα EWs and little to no N V emission in their rest UV spectra.

As is evident in Figure 10, these objects have very high luminosity in the Ly α lines. Konno et al. (2016) demonstrated that, at $z \sim 2$, the majority of the Lyα emitters with Lyα luminosities L (Lyα) $\gtrsim 10^{43}$ erg s^{-1} are associated with AGNs, based on their X-ray, UV, and radio properties. Therefore, we tentatively classify all the objects with L (Lyα) $\geq 10^{43}$ erg s^{-1} as possible quasars. All the above twelve objects meet this criterion. We also note that the UV continuum slope of the above composite spectrum is -1.1 ± 0.3, which is closer to the typical value of quasars ($\alpha = -1.5$) than to that of high-z LBGs ($\beta = -2.0$; Stanway et al. 2005, Bouwens et al. 2014). Future deep observations in other wavelengths, such as X-ray, near-IR, and submm, will reveal the true nature of these intriguing sources.

In Figure 11, we plot the HSC $i_{AB} - z_{AB}$ and $z_{AB} - y_{AB}$ colors of all the spectroscopically-identified objects in Paper I and this work, as well as of the previously known quasars recov-
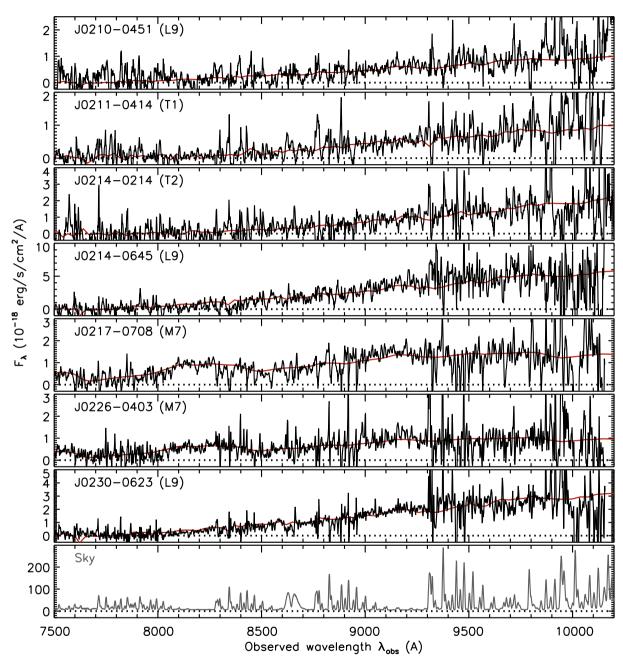
Fig. 7. Same as Figure 2, but for the first seven brown dwarfs. The red lines represent the best-fit templates, whose spectral types are indicated at the top left corner of each panel.
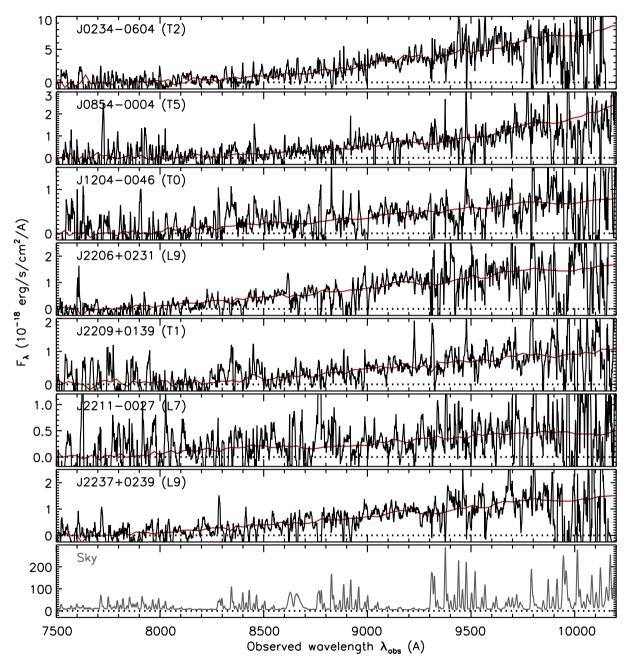
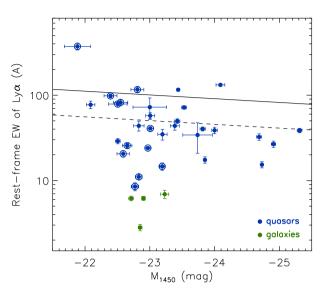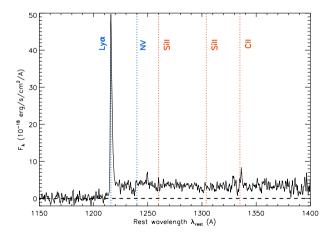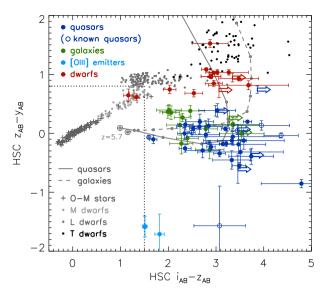**Fig. 8.** Same as Figure 7, but for the remaining seven brown dwarfs.

Fig. 9. The UV absolute magnitudes (M_{1450}) and the rest-frame Lyα EWs of the quasars (blue dots) and the galaxies with clear Lyα emission (green dots). The twelve quasars with narrow Lyα lines are marked with the larger circles. The solid line represents the best-fit relation of AGNs at lower redshifts (Dietrich et al. 2002), while the dashed line represents the same relation modified by IGM absorption, which is assumed to absorb 50 % of the Lyα emission.

Fig. 11. HSC $i_{AB} - z_{AB}$ and $z_{AB} - y_{AB}$ colors of the SHELLQs quasars (blue dots), galaxies (green dots), [O III] emitters (light blue dots), brown dwarfs (red dots), and the previously known quasars recovered in our HSC survey (blue open circles). The grey crosses and dots represent Galactic stars and brown dwarfs, while the solid and dashed lines represent models for quasars and galaxies at $z \geq 5.7$; the dots along the lines represent redshifts in steps of 0.1, with $z = 5.7$ marked by the large open circles. All but the two sources at $z > 6.5$ (which have no reliable i_{AB} and z_{AB} measurements) discovered in Paper I and this work are plotted.

ered in our HSC survey. The quasars are clearly separated from the Galactic stellar sequence on this plane. Their colors are broadly consistent with those of the quasar model we assumed in the Bayesian algorithm, while there are outliers with very blue $z_{AB} - y_{AB}$ colors, due to exceptionally large Lyα EWs.

Figure 12 displays the absolute magnitudes M_{1450} of our new quasars and galaxies (described below), along with those of high-z quasars discovered previously by the other surveys. This figure demonstrates clearly that we are opening up a new parameter space, by finding a large number of objects in the poorly-populated luminosity range of $M_{1450} > -25$ mag at $z > 5.7$.

Figure 13 presents the source extendedness, defined as the difference between the PSF magnitudes (m_{AB}) and CModel magnitudes ($m_{CModel,AB}$). Note that some objects exceed our extendedness cut ($m_{AB} - m_{CModel,AB} < 0.15$), because they had smaller extendedness in the older HSC data releases or they were selected with our previous, looser cut ($m_{AB} - m_{CModel,AB} < 0.30$; see Paper I). It is notable that the objects at the faintest magnitudes have a long tail of the distribution toward extended objects. While some of these objects may have resolved host galaxies, we found that the observed distribution is consistent with that expected for simple point sources, due to photometry errors. We test this with a special HSC dataset, which was created by stacking a part of the SSP UltraDeep data on the COSMOS field to simulate the median depth of the Wide

Fig. 10. Stacked spectrum of the twelve high-z quasars with narrow Lyα lines, presented in the rest frame of the quasars. The dotted lines mark the expected positions of the Lyα, N V λ1240, Si II λ1260, Si II λ1304, and C II λ1335 lines.
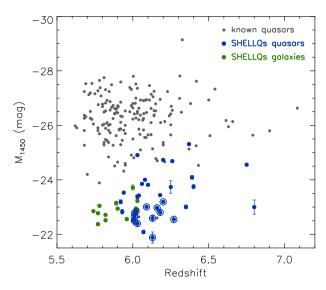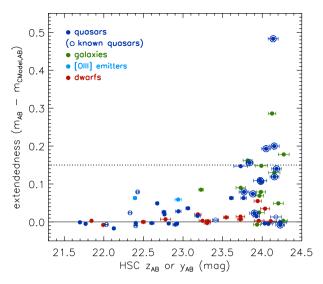
Fig. 12. Rest-UV absolute magnitude at 1450 Å (M_{1450}), as a function of redshift, of the SHELLQs quasars (blue dots) and galaxies (green dots), as well as of all the previously known quasars in the literature (small grey dots). The SHELLQs quasars with narrow Lyα lines are marked with the larger circles. All the high-z objects discovered in Paper I and this work are plotted.

Fig. 13. Source extendedness defined as the difference between the PSF and CModel magnitudes, as a function of the HSC magnitudes (z_{AB} for i-band dropouts and y_{AB} for z-band dropouts), for the SHELLQs quasars (blue dots), galaxies (green dots), [O III] emitters (light blue dots), and brown dwarfs (red dots), and the previously known quasars recovered in our HSC survey (blue open circles). The SHELLQs quasars with narrow Lyα lines are marked with the larger circles. All the sources discovered in Paper I and this work are plotted. The dotted line represents the extendedness cut ($m_{AB} - m_{CModel,AB} < 0.15$) of our quasar selection; note that some objects exceed this limit, since they were selected with the older HSC photometry or with our previous selection threshold (see text).

layer. We selected stars based on the *Hubble Space Telescope* (*HST*) Advanced Camera for Surveys (ACS) catalog (Leauthaud et al. 2007), and measured their HSC extendedness distribution. We found that the fraction of stars with $z_{AB} - z_{CModel,AB} > 0.15$ increases toward faint magnitudes, and approaches $\sim 20\%$ at $z_{AB} = 24.0$ mag. This is roughly consistent with the distribution in Figure 13, where four out of twenty quasars at $23.5 - 24.5$ mag have $z_{AB} - z_{CModel,AB} > 0.15$. No clear correlation is observed between the extendedness values and the PSF widths of the HSC images.

4.2 Galaxies

The eight objects presented in Figure 4 have neither a broad nor a luminous ($> 10^{43}$ erg s^{-1}) Lyα line, and hence are most likely galaxies at $z \sim 6$. Combined with the similar objects presented in Paper I, we have now spectroscopically identified fourteen such objects. Their flat spectra at $\gtrsim 8500$ Å separate them clearly from Galactic brown dwarfs. As we discussed in Paper I, the steep spectral rise around ~ 8500 Å (which is responsible for the very red HSC $i_{AB} - z_{AB}$ colors) of these objects preclude the possibility that they are passive galaxies at $z \sim 1$, which would require unusually large amounts of dust extinction ($E_{B-V} > 1.5$) for such type of galaxies.

The redshifts of these objects were derived from the observed positions of the Lyα emission, the interstellar absorptions of Si II λ1260, Si II λ1304, C II λ1335, and/or the continuum break caused by the IGM H I absorption. However, this is not always easy with our spectra, due to the relatively poor S/N. Thus the redshifts reported here must be regarded as only
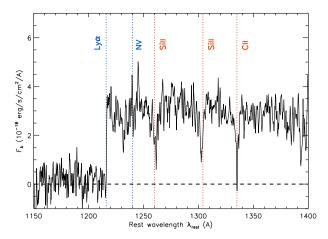
approximate.

The HSC colors of these galaxies are almost indistinguishable from those of the high-z quasars, because of (1) the similar intrinsic rest-UV SEDs of the two populations and (2) the similar effect of the extrinsic IGM absorption. However, the weaker Lyα emission lines make the galaxies mildly redder than the quasars, as seen in Figure 11. The galaxies may be partly resolved with the HSC angular resolution, as they have relatively large $m_{AB} - m_{CModel,AB}$ values (Figure 13). But a similar level of extendedness is found among the faint quasars, due to photometry errors and/or resolved host galaxies as discussed in §4.1, so a clear distinction between these two types of objects remains very difficult with the HSC data alone.

We measured the rest-frame UV absolute magnitudes M_{1450} of these objects in the same way as for the quasars, assuming the continuum slope of $\beta = -2.0$ ($F_\lambda \propto \lambda^\beta$; Stanway et al. 2005). We also measured the Lyα properties for the objects with Lyα lines detected in the spectra. The results of these measurements are summarized in Table 4. These high-z galaxies have extremely high luminosities, in the range of $-24 \lesssim M_{1450} \lesssim -22$ mag. They are even brighter than the galaxies identified in recent studies to constrain the bright end of the galaxy luminosity function at $z \sim 6$, which has now been measured at $M_{1500} \gtrsim -22.5$ mag (e.g., Bouwens et al. 2015; Bowler et al. 2015). Therefore, the high-z galaxies discovered

Fig. 14. Stacked spectrum of the fourteen high-z galaxies, presented in the rest frame of the galaxies. The dotted lines mark the expected positions of the Lyα, N V λ1240, Si II λ1260, Si II λ1304, and C II λ1335 lines.

by our survey have the potential to provide an important clue as to the formation and evolution of most luminous galaxies in the early Universe.

Figure 14 presents the composite spectrum of all the fourteen high-z galaxies we discovered so far. The individual spectra were converted to the rest frame and normalized to $M_{1450} = -22.5$ mag, and then stacked together with inverse-variance weighting. Since redshifts of the galaxies, those without Lyα lines in particular, cannot be determined accurately, any spectral features of the individual spectra are smeared in this composite. Nonetheless, we detected strong absorption lines of Si II λ1260, Si II λ1304, and C II λ1335, whose rest-frame EWs are 2.0 ± 0.5 Å, 1.3 ± 0.4 Å, 2.3 ± 0.4 Å, respectively. These are broadly consistent with the EWs measured in the composite spectrum of $z \sim 3$ LBGs presented by Shapley et al. (2003). The UV spectral slope of our composite spectrum is $\beta = -1.8 \pm 0.1$, which is close to the commonly-assumed value of $\beta = -2.0$ (Stanway et al. 2005).

We note that there is a separate project to search for high-z galaxies from the HSC-SSP dataset (Ono et al. 2017). They apply no extendedness cut in the sample selection, which is complementary to our quasar selection. In addition, Shibuya et al. (2017) are carrying out spectroscopic observations of the HSC sources with excess brightness in narrow-band filters, in the SSP Deep and UltraDeep fields. They have already identified 21 Lyα emitters (LAEs) at $z = 6 - 7$, with high Lyα luminosities and equivalent widths. These LAEs may partly overlap with the population of possible quasars with narrow Lyα discussed above, but a detailed cross comparison is beyond the scope of this paper. Combining the present results with the above works will provide a more complete census of the high-z Universe, covering a wide range of galaxy properties.

4.3 [O III] Emitters

Unexpectedly, we identified two strong [O III] emitters among the quasar candidates, as presented in Figures 6. We measured the line properties of Hγ, Hβ, [O III] λ4959 and λ5007 of these objects, and listed the results in Table 4. Since they have very weak continua, we estimated the continuum levels by summing up all the available pixels except for the above emission lines. Their very high [O III] λ5007/Hβ ratios (log ([O III] λ5007/Hβ) ~ 0.8) are achievable only in galaxies with sub-solar metallicity and high ionization state of the interstellar medium (e.g., Kewley et al. 2016). Since the theoretical prediction of Kewley et al. (2016) doesn't exceed log ([O III] λ5007/Hβ) = 0.7 in all the assumed cases, there may be AGN contribution in our [O III] emitters. Alternatively, they may be extreme emission-line galaxies with compact morphology and low metallicity, which are know to exhibit unusually high [O III] EWs and [O III]/Hβ ratios (Amorín et al. 2014; Amorín et al. 2015). The Hγ/Hβ ratios of these objects are close to the intrinsic value of 0.47 (Osterbrock & Ferland 2006), which indicates that there is little dust extinction.
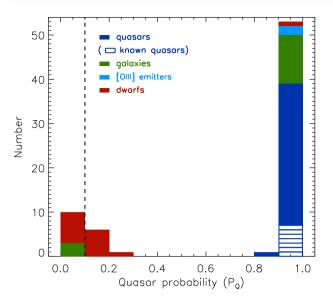
4.4 Brown Dwarfs

We found 14 new brown dwarfs, as presented in Figures 7 and 8. We derived their spectral classes by fitting the spectral standard templates of M4- to T8-type dwarfs, taken from the SpeX Prism Spectral Library (Burgasser 2014; Skrzypek et al. 2015), to the observed spectra at $\lambda_{\rm obs} = 7500 - 9800$ Å. The results are summarized in Table 5 and plotted in Figures 7 and 8. Due to the relatively low S/N and limited spectral coverage, we regard the spectral classes presented here as only approximate. Table 5 also reports the spectral class of $J0850 + 0012$, the one brown dwarf presented in Paper I. These brown dwarfs are of the late-M to T types, which are exactly what we assumed as major contaminants in the quasar selection algorithm.

We note that there are other HSC-SSP projects to look for faint brown dwarfs (Chiang et al., in prep.; Sorahana et al., in prep). Combined with the results from these projects, the present brown dwarfs will provide important clues as to the nature of the Galaxy, such as star-formation history, initial mass function, and spatial structure.

4.5 Survey Efficiency

The efficiency of our high-z quasar survey remains quite high. We have identified the nature of 64 HSC sources in Paper I and this work, which include 33 high-z quasars, 14 high-z galaxies, 2 [O III] emitters, and 15 brown dwarfs. In addition to the above objects, we took follow-up images or spectra of 13 quasar candidates, but they were not detected for unknown reasons. Since they should have been detected with our exposure times based

Fig. 15. Histogram of the Bayesian quasar probability (P_Q^B) of the SHELLQs quasars (blue), galaxies (green), [O III] emitters (light blue), brown dwarfs (red), and the previously known quasars recovered in our HSC survey (white with blue outline). All the sources discovered in Paper I and this work are counted. The dashed line represents our quasar selection threshold ($P_Q^B > 0.1$); note that several objects have lower P_Q^B values than this threshold, because they were selected with older HSC data releases, which indicated higher P_Q^B values.

on the HSC magnitudes, they are most likely transient or moving sources. We are still investigating what these sources could be, and will present the results in a forthcoming paper.

Figure 15 displays a histogram of the Bayesian quasar probability (P_Q^B), for all the spectroscopically identified objects in Paper I and this work. As we mentioned previously, the P_Q^B values have a clear bimodal distribution. The peak at around $P_Q^B = 0.0$ is populated mostly by brown dwarfs, which means that we knew, before spectroscopy, that these HSC sources were not very promising quasar candidates. Many of these dwarfs have lower P_Q^B values than our quasar selection threshold ($P_Q^B = 0.1$), due to the improved HSC photometry with the new data reduction pipeline; we took their spectra because they had $P_Q^B > 0.1$ in the older data releases.

The other peak of the distribution at around $P_Q^B = 1.0$ is populated mostly by high-z quasars. All the discovered quasars have $P_Q^B > 0.8$, which implies that their spectral diversity is reasonably covered by the quasar model in our Bayesian probabilistic algorithm. Figure 15 suggests that we could further improve the success rate of quasar discovery, by raising the selection threshold to, e.g., $P_Q^B = 0.5$. However, we will keep the present threshold for the time being, as we continue the survey, so that we do not miss any quasars with unusual (and thus potentially interesting) spectral properties.

Figure 13 demonstrates that our present extendedness cut ($m_{AB} - m_{CModel,AB} < 0.15$) does not recover all the possible quasars in the HSC survey. Four out of the twenty quasars

with 23.5 – 24.5 mag have larger extendedness, which is consistent with the distribution of the *HST*/ACS stars, as described in §4.1. The exact value of this extendedness cut should be defined as a compromise between completeness and purity of quasar selection, given the available amount of telescope time for spectroscopic identification, and we think the present cut is a reasonable choice for our survey. Of course, the above $\sim$20 % loss of point sources due to the extendedness cut should be corrected for when we measure the luminosity function and other statistical properties.

Contamination by high-z galaxies significantly reduces the purity of quasars among the photometric candidates at the faintest magnitudes (e.g., Figure 13). As we discussed in §4.2, it is difficult in practice to distinguish high-z quasars and galaxies with the HSC photometry data only. However, those bright galaxies are a very useful probe of the Universe in the reionization era. They are excellent targets to study stellar populations at high redshift, with deep optical and near-IR follow-up observations. We also plan to measure their gas and dust properties using, e.g., the Atacama Large Millimeter and sub-millimeter Array (ALMA). We will continue to produce a sample of such galaxies from our survey at $z_{AB} \lesssim 24.5$ mag; at fainter magnitudes, galaxies outnumber quasars and we would need prohibitively large amounts of telescope time to find quasars among the large number of galaxy targets.

4.6 Gravitational Lensing

Given the high probability of gravitational lensing magnification for high-z objects (e.g., Wyithe et al. 2011), it is worthwhile to check the possibility of lensing magnifications for the sample of objects presented in this paper. We did so by cross-correlating our high-z quasars and galaxies with potential foreground deflectors, such as massive galaxies and clusters of galaxies. In the present work, we used two catalogs of HSC foreground objects available at $z < 1.1$. First, we used an HSC cluster catalog with richness $N > 15$ and in the redshift interval $0.1 < z < 1.1$ (Oguri et al. 2017), and found that there are no matches within $60''$. Second, we used a photometric luminous red galaxy sample with stellar mass $M_* > 10^{10.3} M_\odot$ and at redshift $0.05 < z < 1.05$ (Oguri et al., in prep.), and found 7 matches within $10''$. We estimated magnifications by these nearby red galaxies by converting the stellar masses to stellar velocity dispersions, using the scaling relation derived in SDSS (Kauffmann et al. 2003), and adopting a singular isothermal sphere for the mass distribution of the individual galaxies. We found that the magnification factors by these galaxies are small, $\mu \lesssim 1.2$ at most. A potentially interesting object is the galaxy $J2233+0124$; there is a red galaxy at $z \sim 0.66$ with an angular separation of $1''.9$, and there is also a cluster of galaxies with richness $N \sim 15$ at the similar redshift, $z \sim 0.65$, at a separa-

tion of $\sim 90''$. However, the magnification by these foreground sources is estimated to be small, assuming the standard scaling relations between galaxy properties and underlying mass distribution.

Although the above analysis does not test all the potential deflectors, we conclude for now that there is no evidence of lensing magnification at work in the present sample of high-z quasars and galaxies. A more effective test will be to observe these objects with higher angular resolution, e.g., with the *HST* or the *James Webb Space Telescope*, to look for lensed morphology or companion. We note that Richards et al. (2004,2006) carried out a *HST*/ACS snapshot survey of SDSS quasars, but found no case of strong lensing in 161 quasars at $4.0 < z < 6.4$.

5 Summary

This paper is the second in a series presenting the results of the SHELLQs project, a survey of low-luminosity quasars at high redshift ($z > 5.7$) close to the reionization era. Quasar candidates are selected with a Bayesian probabilisitic algorithm, using the multi-band imaging data of the Subaru HSC-SSP survey. We took optical spectra of 48 candidates with GTC/OSIRIS and Subaru/FOCAS, and newly discovered 24 quasars and 8 luminous galaxies at $5.7 < z \leq 6.8$. Combined with the sample presented in Paper I, we have now identified 64 HSC sources over about 430 deg^2, which include 33 high-z quasars, 14 high-z luminous galaxies, 2 [O III] emitters at $z \sim 0.8$, and 15 Galactic brown dwarfs. We present a spectral analysis of all these objects in this paper.

The new quasars have considerably lower luminosity ($M_{1450} \sim -25$ to -22 mag) than most of the previously known high-z quasars. Several of these quasars have luminous ($> 10^{43}$ erg s^{-1}) and narrow (< 500 km s^{-1}) Lyα lines, and also a possible mini BAL system of N v λ1240 in the composite spectrum, which clearly separate them from typical quasars. On the other hand, the high-z galaxies have extremely high luminosity ($M_{1450} \sim -24$ to -22 mag) compared to other galaxies found at similar redshift. With the discovery of these new classes of objects, we are opening up new parameter spaces in the high-z Universe. The two [O III] emitters are likely to be low-metallicity star-forming galaxies at $z \sim 0.8$, but there may be AGN contribution to the very strong [O III] lines. The brown dwarfs have the spectral classes from late-M to T, which are exactly what we assumed as major contaminants in the quasar selection algorithm. Our survey remains quite efficient, with most of the objects with significant Bayesian quasar probability ($P_Q^B > 0.5$) being identified as high-z quasars or galaxies spectroscopically.

The SHELLQs project will continue, as the HSC-SSP survey continues toward its goals of observing 1400 deg^2 in the Wide layer, as well as 27 and 3.5 deg^2 in the Deep and UltraDeep layer, respectively. We expect to discover $\sim$500 quasars with $z_{AB} < 24.5$ mag at $z \sim 6$, and $\sim$100 quasars with $y_{AB} < 24.0$ mag at $z \sim 7$, in the entire Wide field (see Paper I). No other survey has an ability to find such a large sample of high-z low-luminosity quasars, before the advent of Large Synoptic Survey Telescope. We are discovering more new quasars while this paper is written, which will be reported in forthcoming papers. We will also derive our first quasar luminosity function at $z \sim 6$, reaching down to $M_{AB} \sim -22$ mag, very soon. Follow-up observations of the discovered objects are being considered at various wavelengths from sub-millimeter/radio to X-ray. Several of them have already been observed with ALMA and near-IR spectrographs on the Gemini telescope and Very Large Telescope, whose results will be presented elsewhere.

References

Abazajian, K., Adelman-McCarthy, J. K., Agüeros, M. A., et al. 2004, AJ, 128, 502

Aihara, H., Armstrong, R., Bickerton, S., et al. 2017, arXiv:1702.08449

Alexandroff, R., Strauss, M. A., Greene, J. E., et al. 2013, MNRAS, 435, 3306

Amorín, R., Pérez-Montero, E., Contini, T., et al. 2015, A&A, 578, A105

Amorín, R., Sommariva, V., Castellano, M., et al. 2014, A&A, 568, L8

Bañados, E., Venemans, B. P., Decarli, R., et al. 2016, ApJS, 227, 11

Bañados, E., Venemans, B. P., Morganson, E., et al. 2014, AJ, 148, 14

Bertin, E., & Arnouts, S. 1996, A&AS, 117, 393

Bouwens, R. J., Illingworth, G. D., Oesch, P. A., et al. 2014, ApJ, 793, 115

Bouwens, R. J., Illingworth, G. D., Oesch, P. A., et al. 2015, ApJ, 803, 34

Bowler, R. A. A., Dunlop, J. S., McLure, R. J., et al. 2015, MNRAS, 452, 1817

Burgasser, A. J. 2014, Astronomical Society of India Conference Series, 11,

Carnall, A. C., Shanks, T., Chehade, B., et al. 2015, MNRAS, 451, L16

Cepa, J., Aguiar, M., Escalera, V. G., et al. 2000, Proc. SPIE, 4008, 623

Chambers, K. C., Magnier, E. A., Metcalfe, N., et al. 2016, arXiv:1612.05560

Dark Energy Survey Collaboration, Abbott, T., Abdalla, F. B., et al. 2016, arXiv:1601.00329

Dietrich, M., Hamann, F., Shields, J. C., et al. 2002, ApJ, 581, 912

Fan, X., Carilli, C. L., & Keating, B. 2006, ARA&A, 44, 415

Fan, X., Hennawi, J. F., Richards, G. T., et al. 2004, AJ, 128, 515

Fan, X., Narayanan, V. K., Lupton, R. H., et al. 2001, AJ, 122, 2833

Fan, X., Strauss, M. A., Richards, G. T., et al. 2006, AJ, 131, 1203

Fan, X., Strauss, M. A., Schneider, D. P., et al. 2003, AJ, 125, 1649

Fan, X., White, R. L., Davis, M., et al. 2000, AJ, 120, 1167

Ferrara, A., Salvadori, S., Yue, B., & Schleicher, D. 2014, MNRAS, 443, 2410

Flewelling, H. A., Magnier, E. A., Chambers, K. C., et al. 2016, arXiv:1612.05243

Fukugita, M., Ichikawa, T., Gunn, J. E., et al. 1996, AJ, 111, 1748

Goto, T. 2006, MNRAS, 371, 769

Gunn, J. E., & Peterson, B. A. 1965, ApJ, 142, 1633

Hall, P. B., Hoversten, E. A., Tremonti, C. A., et al. 2004, AJ, 127, 3146

Jiang, L., Fan, X., Annis, J., et al. 2008, AJ, 135, 1057

Jiang, L., Fan, X., Bian, F., et al. 2009, AJ, 138, 305

Jiang, L., McGreer, I. D., Fan, X., et al. 2015, AJ, 149, 188

Jiang, L., McGreer, I. D., Fan, X., et al. 2016, ApJ, 833, 222

Jurić, M., Kantor, J., Lim, K., et al. 2015, arXiv:1512.07914

Kashikawa, N., Aoki, K., Asai, R., et al. 2002, PASJ, 54, 819

Kashikawa, N., Ishizaki, Y., Willott, C. J., et al. 2015, ApJ, 798, 28

Kaiser, N., Burgett, W., Chambers, K., et al. 2010, Proc. SPIE, 7733, 77330E

Kauffmann, G., Heckman, T. M., White, S. D. M., et al. 2003, MNRAS, 341, 33

Kewley, L. J., Yuan, T., Nanayakkara, T., et al. 2016, ApJ, 819, 100

Kim, Y., Im, M., Jeon, Y., et al. 2015, ApJL, 813, L35

Konno, A., Ouchi, M., Nakajima, K., et al. 2015, arXiv:1512.01854

Lawrence, A., Warren, S. J., Almaini, O., et al. 2007, MNRAS, 379, 1599

Leauthaud, A., Massey, R., Kneib, J.-P., et al. 2007, ApJS, 172, 219

Madau, P., Haardt, F., & Dotti, M. 2014, ApJL, 784, L38

Magnier, E. A., Schlafly, E., Finkbeiner, D., et al. 2013, ApJS, 205, 20

Mainieri, V., Rigopoulou, D., Lehmann, I., et al. 2005, MNRAS, 356, 1571

Martínez-Sansigre, A., Rawlings, S., Lacy, M., et al. 2006, MNRAS, 370, 1479

Matsuoka, Y., Onoue, M., Kashikawa, N., et al. 2016, ApJ, 828, 26 (Paper I)

McCarthy, P. J. 1993, ARA&A, 31, 639

Miyazaki, S., Komiyama, Y., Nakaya, H., et al. 2012, Proc. SPIE, 8446, 84460Z

Mortlock, D. J., Patel, M., Warren, S. J., et al. 2012, MNRAS, 419, 390

Mortlock, D. J., Warren, S. J., Venemans, B. P., et al. 2011, Nature, 474, 616

Oguri, M., Lin, Y.-T., Lin, S.-C., et al. 2017, arXiv:1701.00818

Oke, J. B., & Gunn, J. E. 1983, ApJ, 266, 713

Ono, Y., Ouchi, M., Harikane, Y., et al. 2017, arXiv:1704.06004

Osterbrock, D. E., & Ferland, G. J. 2006, Astrophysics of gaseous nebulae and active galactic nuclei, 2nd. ed. by D.E. Osterbrock and G.J. Ferland. Sausalito, CA: University Science Books, 2006,

Pickles, A. J. 1998, PASP, 110, 863

Reed, S. L., McMahon, R. G., Banerji, M., et al. 2015, MNRAS, 454, 3952

Reed, S. L., McMahon, R. G., Martini, P., et al. 2017, arXiv:1701.04852

Richards, G. T., Fan, X., Newberg, H. J., et al. 2002, AJ, 123, 2945

Richards, G. T., Haiman, Z., Pindor, B., et al. 2006, AJ, 131, 49

Richards, G. T., Strauss, M. A., Pindor, B., et al. 2004, AJ, 127, 1305

Schlafly, E. F., Finkbeiner, D. P., Jurić, M., et al. 2012, ApJ, 756, 158

Schlegel, D. J., Finkbeiner, D. P., & Davis, M. 1998, ApJ, 500, 525

Shapley, A. E., Steidel, C. C., Pettini, M., & Adelberger, K. L. 2003, ApJ, 588, 65

Shibuya, T., Ouchi, M., Harikane, Y., et al. 2017, arXiv:1705.00733

Skrzypek, N., Warren, S. J., Faherty, J. K., et al. 2015, A&A, 574, A78

Songaila, A. 2004, AJ, 127, 2598

Stanway, E. R., McMahon, R. G., & Bunker, A. J. 2005, MNRAS, 359, 1184

Stern, D., Moran, E. C., Coil, A. L., et al. 2002, ApJ, 568, 71

Tonry, J. L., Stubbs, C. W., Lykke, K. R., et al. 2012, ApJ, 750, 99

Vanden Berk, D. E., Richards, G. T., Bauer, A., et al. 2001, AJ, 122, 549

Venemans, B. P., Bañados, E., Decarli, R., et al. 2015, ApJL, 801, L11

Venemans, B. P., Findlay, J. R., Sutherland, W. J., et al. 2013, ApJ, 779, 24

Venemans, B. P., Verdoes Kleijn, G. A., Mwebaze, J., et al. 2015, MNRAS, 453, 2259

Volonteri, M. 2012, Science, 337, 544

Wang, F., Fan, X., Yang, J., et al. 2017, arXiv:1703.07490

Willott, C. J., Delfosse, X., Forveille, T., Delorme, P., & Gwyn, S. D. J. 2005, ApJ, 633, 630

Willott, C. J., Delorme, P., Omont, A., et al. 2007, AJ, 134, 2435

Willott, C. J., Albert, L., Arzoumanian, D., et al. 2010a, AJ, 140, 546

Willott, C. J., Delorme, P., Reylé, C., et al. 2010b, AJ, 139, 906

Willott, C. J., Delorme, P., Reylé, C., et al. 2009, AJ, 137, 3541

Wu, X.-B., Wang, F., Fan, X., et al. 2015, Nature, 518, 512

Wyithe, J. S. B., Yan, H., Windhorst, R. A., & Mao, S. 2011, Nature, 469, 181

York, D. G., Adelman, J., Anderson, J. E., Jr., et al. 2000, AJ, 120, 1579

Table 1. Journal of Discovery Observations

Target	Exp. Time	Date	Telescope
$J1429 - 0104$	300 min	2016 May 2, 13, Jun 27, 30	GTC
$J0857 + 0056$	120 min	2016 Feb 12, 14	Subaru
$J0905 + 0300$	60 min	2016 Feb 13	Subaru
$J2239 + 0207$	15 min	2016 Jun 8	GTC
$J0844 - 0052$	60 min	2016 Apr 9	GTC
$J1208 - 0200$	30 min	2016 Feb 13	Subaru
$J0217 - 0208$	60 min	2016 Sep 9	Subaru
$J1425 - 0015$	180 min	2016 Feb 12, 14, 16	Subaru
$J2201 + 0155$	80 min	2016 Sep 7	Subaru
$J1423 - 0018$	120 min	2016 Feb 14, 16	Subaru
$J1440 - 0107$	40 min	2016 Feb 13	Subaru
$J0235 - 0532$	60 min	2016 Sep 7	Subaru
$J2228 + 0152$	30 min	2016 Jun 27	GTC
$J0911 + 0152$	120 min	2016 Feb 15, 16	Subaru
$J1201 + 0133$	120 min	2016 Feb 12, 14	Subaru
$J1429 - 0002$	60 min	2016 Feb 12	Subaru
$J0202 - 0251$	45 min	2016 Aug 10	GTC
$J0206 - 0255$	15 min	2016 Jul 30	GTC
$J1416 + 0015$	60 min	2016 Feb 14	Subaru
$J1417 + 0117$	60 min	2016 Feb 13	Subaru
$J0902 + 0155$	160 min	2016 Feb 12, 14	Subaru
$J0853 + 0139$	30 min	2016 Feb 15	Subaru
$J1414 + 0130$	60 min	2016 Apr 13	GTC
$J0903 + 0211$	120 min	2016 Apr 3, 24	GTC
$J1628 + 4312$	170 min	2016 Feb 13, 15, 16	Subaru
$J1211 - 0118$	60 min	2016 Apr 28	GTC
$J1630 + 4315$	45 min	2016 Feb 14	Subaru
$J2233 + 0124$	60 min	2016 Sep 9	Subaru
$J0212 - 0158$	60 min	2016 Aug 27	GTC
$J0218 - 0220$	60 min	2016 Sep 7	Subaru
$J0159 - 0359$	60 min	2016 Sep 9	Subaru
$J2237 - 0006$	100 min	2016 Sep 9	Subaru
$J1157 - 0157$	45 min	2016 Apr 9	GTC
$J1443 - 0214$	15 min	2016 May 5	GTC
$J0210 - 0451$	25 min	2016 Sep 7	Subaru
$J0211 - 0414$	135 min	2015 Sep 9, 12	GTC
$J0214 - 0214$	15 min	2016 Sep 7	Subaru
$J0214 - 0645$	15 min	2016 Jul 31	GTC
$J0217 - 0708$	135 min	2015 Sep 12, 14	GTC
$J0226 - 0403$	90 min	2015 Sep 12	GTC
$J0230 - 0623$	135 min	2015 Sep 8	GTC
$J0234 - 0604$	15 min	2016 Aug 2	GTC
$J0854 - 0004$	40 min	2016 Feb 12	Subaru
$J1204 - 0046$	45 min	2016 Feb 15	Subaru
$J2206 + 0231$	60 min	2016 Jun 9	GTC
$J2209 + 0139$	20 min	2016 Sep 7	Subaru
$J2211 - 0027$	25 min	2016 Sep 7	Subaru
$J2237 + 0239$	60 min	2016 Jun 30	GTC

Table 2. Photometric properties

Name	R.A.	Decl.	i_{AB} (mag)	z_{AB} (mag)	y_{AB} (mag)	P_Q^B
		High-z Quasars				
$J1429-0104$	14:29:03.08	-01:04:43.4	>26.61	>25.25	23.73 ± 0.09	0.86
$J0857+0056$	08:57:38.53	$+00$:56:12.7	27.43 ± 0.97	24.08 ± 0.05	24.14 ± 0.14	1.00
$J0905+0300$	09:05:44.65	$+03$:00:58.8	26.94 ± 0.29	24.16 ± 0.06	24.18 ± 0.14	1.00
$J2239+0207$	22:39:47.47	$+02$:07:47.5	25.60 ± 0.09	22.40 ± 0.01	22.33 ± 0.03	1.00
$J0844-0052$	08:44:31.60	-00:52:54.6	>25.65	23.18 ± 0.03	23.12 ± 0.08	1.00
$J1208-0200$	12:08:59.23	-02:00:34.8	24.65 ± 0.08	22.13 ± 0.02	22.05 ± 0.03	1.00
$J0217-0208$	02:17:21.59	-02:08:52.6	>25.88	23.88 ± 0.04	23.50 ± 0.08	1.00
$J1425-0015$	14:25:17.72	-00:15:40.9	26.30 ± 0.14	22.82 ± 0.02	23.37 ± 0.05	1.00
$J2201+0155$	22:01:32.07	$+01$:55:29.0	27.49 ± 0.89	23.98 ± 0.08	24.29 ± 0.19	1.00
$J1423-0018$	14:23:31.71	-00:18:09.1	>26.64	24.18 ± 0.06	24.79 ± 0.23	1.00
$J1440-0107$	14:40:01.30	-01:07:02.2	26.98 ± 0.41	24.14 ± 0.06	24.01 ± 0.10	1.00
$J0235-0532$	02:35:42.42	-05:32:41.6	27.24 ± 0.57	23.77 ± 0.06	23.96 ± 0.15	1.00
$J2228+0152$	22:28:47.71	$+01$:52:40.5	25.57 ± 0.09	22.67 ± 0.02	22.91 ± 0.04	1.00
$J0911+0152$	09:11:14.27	$+01$:52:19.4	27.81 ± 0.84	24.22 ± 0.08	24.35 ± 0.13	1.00
$J1201+0133$	12:01:03.02	$+01$:33:56.4	>25.53	22.94 ± 0.03	23.31 ± 0.09	1.00
$J1429-0002$	14:29:20.22	-00:02:07.4	26.00 ± 0.12	22.93 ± 0.02	23.27 ± 0.05	1.00
$J0202-0251$	02:02:58.21	-02:51:53.6	26.39 ± 0.30	23.06 ± 0.03	23.18 ± 0.04	1.00
$J0206-0255$	02:06:11.20	-02:55:37.8	24.84 ± 0.07	21.70 ± 0.01	21.88 ± 0.02	1.00
$J1416+0015$	14:16:12.71	$+00$:15:46.2	27.18 ± 0.38	24.15 ± 0.06	23.76 ± 0.10	1.00
$J1417+0117$	14:17:28.67	$+01$:17:12.4	26.56 ± 0.28	23.90 ± 0.06	23.71 ± 0.12	1.00
$J0902+0155$	09:02:54.87	$+01$:55:10.9	26.75 ± 0.36	24.03 ± 0.04	24.32 ± 0.12	1.00
$J0853+0139$	08:53:48.84	$+01$:39:11.0	26.88 ± 0.47	24.23 ± 0.06	24.12 ± 0.11	1.00
$J1414+0130$	14:14:39.54	$+01$:30:36.5	25.26 ± 0.12	22.90 ± 0.03	23.16 ± 0.06	1.00
$J0903+0211$	09:03:14.68	$+02$:11:28.3	25.30 ± 0.07	23.61 ± 0.03	23.71 ± 0.07	1.00
$J1205-0000^*$	12:05:05.09	-00:00:27.9	>26.61	>25.92	22.61 ± 0.03	1.00
$J2236+0032^*$	22:36:44.58	$+00$:32:56.8	>26.94	23.93 ± 0.04	23.19 ± 0.05	1.00
$J0859+0022^*$	08:59:07.19	$+00$:22:55.9	27.55 ± 0.84	22.77 ± 0.01	23.62 ± 0.07	1.00
$J1152+0055^*$	11:52:21.27	$+00$:55:36.6	25.43 ± 0.09	21.77 ± 0.01	21.57 ± 0.02	1.00
$J2232+0012^*$	22:32:12.03	$+00$:12:38.4	27.58 ± 0.47	23.84 ± 0.05	24.23 ± 0.13	1.00
$J2216-0016^*$	22:16:44.47	-00:16:50.0	25.97 ± 0.15	22.76 ± 0.03	22.94 ± 0.04	1.00
$J2228+0128^*$	22:28:27.83	$+01$:28:09.4	27.38 ± 0.40	24.05 ± 0.05	24.50 ± 0.15	1.00
$J1207-0005^*$	12:07:54.14	-00:05:53.2	26.34 ± 0.16	23.98 ± 0.04	23.83 ± 0.09	1.00
$J1202-0057^*$	12:02:46.37	-00:57:01.6	26.11 ± 0.14	23.77 ± 0.03	23.77 ± 0.10	1.00
		High-z Galaxies				
$J1628+4312$	16:28:33.02	$+43$:12:10.6	27.52 ± 0.47	23.98 ± 0.06	23.99 ± 0.13	1.00
$J1211-0118$	12:11:37.10	-01:18:16.4	>26.27	23.99 ± 0.07	23.97 ± 0.10	1.00
$J1630+4315$	16:30:26.36	$+43$:15:58.6	26.94 ± 0.23	24.15 ± 0.07	24.08 ± 0.13	1.00
$J2233+0124$	22:33:39.34	$+01$:24:32.4	27.07 ± 0.29	24.20 ± 0.06	24.48 ± 0.14	1.00
$J0212-0158$	02:12:44.75	-01:58:24.6	25.53 ± 0.17	23.23 ± 0.03	22.96 ± 0.06	1.00
$J0218-0220$	02:18:03.42	-02:20:29.7	26.40 ± 0.30	23.94 ± 0.04	23.56 ± 0.08	1.00
$J0159-0359$	01:59:49.36	-03:59:45.2	26.24 ± 0.24	23.96 ± 0.06	24.14 ± 0.16	1.00
$J2237-0006$	22:37:13.51	-00:06:12.7	27.62 ± 0.55	24.27 ± 0.05	24.12 ± 0.11	1.00
$J0219-0416^*$	02:19:29.41	-04:16:45.9	>26.49	24.27 ± 0.07	24.01 ± 0.11	1.00
$J0210-0523^*$	02:10:33.82	-05:23:04.3	25.79 ± 0.17	23.73 ± 0.06	23.38 ± 0.10	0.09
$J0857+0142^*$	08:57:23.95	$+01$:42:54.6	26.14 ± 0.25	24.12 ± 0.05	23.73 ± 0.08	0.00
$J0210-0559^*$	02:10:41.28	-05:59:17.9	26.48 ± 0.27	24.24 ± 0.07	24.10 ± 0.16	0.97
$J0848+0045^*$	08:48:18.33	$+00$:45:09.5	26.22 ± 0.22	23.82 ± 0.06	23.90 ± 0.09	1.00
$J0215-0555^*$	02:15:45.20	-05:55:29.0	25.96 ± 0.16	23.97 ± 0.05	23.60 ± 0.10	0.06

Table 2. (Continued)

Name	R.A.	Decl.	i_{AB} (mag)	z_{AB} (mag)	y_{AB} (mag)	$P_{\mathrm{Q}}^{\mathrm{B}}$
			[O III] Emitters			
$J1157 - 0157$	11:57:51.82	-01:57:09.9	24.76 ± 0.09	22.94 ± 0.04	24.65 ± 0.34	1.00
$J1443 - 0214$	14:43:58.26	-02:14:47.3	23.90 ± 0.04	22.39 ± 0.02	23.97 ± 0.18	1.00
			Brown Dwarfs			
$J0210 - 0451$	02:10:47.24	-04:51:03.9	>25.92	23.73 ± 0.06	22.78 ± 0.05	0.14
$J0211 - 0414$	02:11:25.26	-04:14:03.5	26.83 ± 0.37	23.96 ± 0.06	22.43 ± 0.03	0.00
$J0214 - 0214$	02:14:25.22	-02:14:59.0	26.58 ± 0.41	23.32 ± 0.03	22.28 ± 0.03	0.12
$J0214 - 0645$	02:14:32.59	-06:45:22.3	24.80 ± 0.10	21.84 ± 0.02	20.82 ± 0.01	1.00
$J0217 - 0708$	02:17:29.47	-07:08:19.6	23.94 ± 0.07	22.78 ± 0.07	22.14 ± 0.08	0.00
$J0226 - 0403$	02:26:18.44	-04:03:06.7	24.52 ± 0.04	23.19 ± 0.04	22.58 ± 0.04	0.00
$J0230 - 0623$	02:30:46.80	-06:23:56.7	25.39 ± 0.21	22.50 ± 0.03	21.53 ± 0.03	0.14
$J0234 - 0604$	02:34:30.10	-06:04:56.5	24.79 ± 0.10	21.99 ± 0.01	20.91 ± 0.01	0.06
$J0854 - 0004$	08:54:10.91	-00:04:54.7	27.02 ± 0.42	23.54 ± 0.03	22.62 ± 0.03	0.00
$J1204 - 0046$	12:04:49.68	-00:46:17.2	25.97 ± 0.12	23.94 ± 0.05	23.20 ± 0.06	0.00
$J2206 + 0231$	22:06:14.53	$+02$:31:38.9	25.78 ± 0.18	23.25 ± 0.04	22.57 ± 0.05	0.29
$J2209 + 0139$	22:09:06.22	$+01$:39:57.0	26.75 ± 0.24	23.72 ± 0.03	22.69 ± 0.03	0.12
$J2211 - 0027$	22:11:55.16	-00:27:36.1	>26.07	24.11 ± 0.08	23.37 ± 0.11	0.19
$J2237 + 0239$	22:37:12.37	$+02$:39:22.6	26.26 ± 0.18	23.30 ± 0.04	22.46 ± 0.04	0.15
$J0850 + 0012^{*}$	08:50:02.63	$+00$:12:10.0	27.72 ± 0.84	24.04 ± 0.06	23.22 ± 0.05	0.05

Note — Coordinates are at J2000.0. Magnitude upper limits are placed at 5σ significance. Names with * denote the objects taken from Paper I.

Table 3. JHK magnitudes of the objects detected in UKIDSS or VIKING.

Name	UKIDSS			VIKING			Comment
	J_{AB} (mag)	H_{AB} (mag)	K_{AB} (mag)	J_{AB} (mag)	H_{AB} (mag)	K_{AB} (mag)	
$J1205 - 0000^{*}$	...	...	...	21.95 ± 0.21	21.49 ± 0.34	20.73 ± 0.18	high-z quasar
$J1152 + 0055^{*}$	...	...	...	21.66 ± 0.22	...	...	high-z quasar
$J0854 - 0004$	...	...	...	21.27 ± 0.11	21.16 ± 0.28	...	brown dwarf
$J1204 - 0046$	...	...	...	...	20.93 ± 0.21	20.88 ± 0.21	brown dwarf
$J2206 + 0231$	...	20.24 ± 0.22	...	...	...	...	brown dwarf
$J0850 + 0012^{*}$	...	...	20.55 ± 0.27	...	...	...	brown dwarf

* These sources are taken from Paper I.

Table 4. Spectroscopic properties

Name	Redshift[†]	M_{1450}	Line	EW_{rest} (Å)	FWHM (km s^{-1})	$\log L$ (erg s^{-1})
			High-z Quasars			
$J1429-0104$	6.8	-23.00 ± 0.26	Lyα	72 ± 20	1400 ± 100	43.95 ± 0.06
$J0857+0056$	6.35	-23.01 ± 0.07	Lyα	57 ± 5	620 ± 90	43.85 ± 0.02
$J0905+0300$	6.27	-22.55 ± 0.11	Lyα	82 ± 6	250 ± 40	43.89 ± 0.02
$J2239+0207$	6.26	-24.69 ± 0.04	Lyα	32 ± 3	5800 ± 2700	44.27 ± 0.03
$J0844-0052$	6.25	-23.74 ± 0.23	Lyα	34 ± 13	1800 ± 900	43.91 ± 0.14
$J1208-0200$	6.2	-24.73 ± 0.02	Lyα	15 ± 1	5500 ± 1800	43.97 ± 0.04
$J0217-0208$	6.20	-23.19 ± 0.04	Lyα	15 ± 1	< 230	43.33 ± 0.04
$J1425-0015$	6.18	-23.44 ± 0.02	Lyα	116 ± 3	1400 ± 400	44.32 ± 0.01
$J2201+0155$	6.16	-22.97 ± 0.04	Lyα	24 ± 1	320 ± 70	43.46 ± 0.01
$J1423-0018$	6.13	-21.88 ± 0.20	Lyα	370 ± 30	< 230	44.30 ± 0.01
$J1440-0107$	6.13	-22.59 ± 0.10	Lyα	21 ± 2	440 ± 260	43.27 ± 0.03
$J0235-0532$	6.09	-23.01 ± 0.05	Lyα	41 ± 2	270 ± 30	43.68 ± 0.02
$J2228+0152$	6.08	-24.00 ± 0.04	Lyα	39 ± 3	3000 ± 200	44.07 ± 0.03
$J0911+0152$	6.07	-22.09 ± 0.07	Lyα	77 ± 8	6500 ± 4200	43.60 ± 0.04
$J1201+0133$	6.06	-23.85 ± 0.02	Lyα	17 ± 1	1300 ± 600	43.67 ± 0.04
$J1429-0002$	6.04	-23.42 ± 0.04	Lyα	50 ± 3	2900 ± 600	43.95 ± 0.02
$J0202-0251$	6.03	-23.39 ± 0.07	Lyα	44 ± 5	5600 ± 800	43.88 ± 0.04
$J0206-0255$	6.03	-24.91 ± 0.03	Lyα	27 ± 2	5000 ± 500	44.28 ± 0.03
$J1416+0015$	6.03	-22.39 ± 0.10	Lyα	98 ± 5	230 ± 20	43.86 ± 0.01
$J1417+0117$	6.02	-22.83 ± 0.05	Lyα	11 ± 1	420 ± 70	43.06 ± 0.03
$J0902+0155$	6.01	-22.51 ± 0.04	Lyα	29 ± 2	1600 ± 1200	43.35 ± 0.03
$J0853+0139$	6.01	-22.51 ± 0.14	Lyα	79 ± 6	< 230	43.80 ± 0.01
$J1414+0130$	5.94	-23.53 ± 0.04	Lyα	72 ± 3	2400 ± 1900	44.16 ± 0.01
$J0903+0211$	5.92	-23.20 ± 0.07	Lyα	35 ± 5	1400 ± 100	43.70 ± 0.06
$J1205-0000^*$	6.75	-24.56 ± 0.04	...	...	...	...
$J2236+0032^*$	6.4	-23.75 ± 0.07	...	...	...	...
$J0859+0022^*$	6.39	-24.09 ± 0.07	Lyα	130 ± 5	540 ± 110	44.52 ± 0.01
			NV	38 ± 2	1800 ± 200	43.97 ± 0.02
$J1152+0055^*$	6.37	-25.31 ± 0.04	Lyα	39 ± 2	5500 ± 1900	44.60 ± 0.02
$J2232+0012^*$	6.18	-22.81 ± 0.10	Lyα	120 ± 10	300 ± 30	44.06 ± 0.01
$J2216-0016^*$	6.10	-23.82 ± 0.04	Lyα	40 ± 2	1900 ± 300	44.03 ± 0.02
$J2228+0128^*$	6.01	-22.65 ± 0.07	Lyα	26 ± 2	280 ± 30	43.34 ± 0.02
$J1207-0005^*$	6.01	-22.77 ± 0.06	Lyα	8.5 ± 0.9	420 ± 160	42.92 ± 0.05
$J1202-0057^*$	5.93	-22.83 ± 0.08	Lyα	44 ± 6	1600 ± 700	43.66 ± 0.05
			High-z Galaxies			
$J1628+4312$	6.03	-22.90 ± 0.03	Lyα	6.2 ± 0.3	230 ± 40	42.78 ± 0.02
$J1211-0118$	6.03	-23.23 ± 0.06	Lyα	6.9 ± 0.8	360 ± 230	42.87 ± 0.04
$J1630+4315$	6.02	-22.95 ± 0.04	...	...	...	...
$J2233+0124$	6.0	-22.52 ± 0.09	...	...	...	...
$J0212-0158$	6.0	-23.72 ± 0.09	...	...	...	...
$J0218-0220$	5.9	-22.94 ± 0.04	...	...	...	...
$J0159-0359$	5.77	-22.78 ± 0.05	...	...	...	...
$J2237-0006$	5.77	-22.37 ± 0.05	...	...	...	...
$J0219-0416^*$	5.96	-22.56 ± 0.06	...	...	...	...
$J0210-0523^*$	5.89	-23.14 ± 0.07	...	...	...	...
$J0857+0142^*$	5.82	-22.71 ± 0.04	Lyα	6.2 ± 0.4	400 ± 50	42.67 ± 0.03
$J0210-0559^*$	5.82	-22.52 ± 0.05	...	...	...	...
$J0848+0045^*$	5.78	-23.04 ± 0.05	...	...	...	...

Table 4. (Continued)

Name	Redshift[†]	M_{1450}	Line	EW$_{\rm rest}$ (Å)	FWHM (km s^{-1})	log L (erg s^{-1})
$J0215-0555^*$	5.74	-22.85 ± 0.03	Lyα	2.8 ± 0.2	410 ± 160	42.39 ± 0.04
			[O III] Emitters			
$J1157-0157$	0.810	...	Hγ	190 ± 30	< 190	41.39 ± 0.04
			Hβ	340 ± 40	< 190	41.65 ± 0.01
			[O III] $\lambda4959$	780 ± 100	< 190	42.01 ± 0.01
			[O III] $\lambda5007$	2100 ± 300	< 190	42.44 ± 0.01
$J1443-0214$	0.776	...	Hγ	61 ± 11	< 190	41.30 ± 0.07
			Hβ	130 ± 20	< 190	41.64 ± 0.03
			[O III] $\lambda4959$	320 ± 30	< 190	42.01 ± 0.01
			[O III] $\lambda5007$	940 ± 90	< 190	42.48 ± 0.01

* These sources are taken from Paper I. [†] Recorded to two significant figures when the position of Lyα emission or interstellar absorption is unambiguous.

Table 5. Spectral classes of the brown dwarfs.

Name	Class
$J0210 - 0451$	L9
$J0211 - 0414$	T1
$J0214 - 0214$	T2
$J0214 - 0645$	L9
$J0217 - 0708$	M7
$J0226 - 0403$	M7
$J0230 - 0623$	L9
$J0234 - 0604$	T2
$J0854 - 0004$	T5
$J1204 - 0046$	T0
$J2206 + 0231$	L9
$J2209 + 0139$	T1
$J2211 - 0027$	L7
$J2237 + 0239$	L9
$J0850 + 0012^{*}$	T1

[*]This object is taken from Paper I.